Enhanced electric resistivity and dielectric energy storage by vacancy defect complex

Hao Pan[a,b,1], Nan Feng[c,1], Xing Xu[a], Weiwei Li[d,e], Qinghua Zhang[f], Shun Lan[a], Yi-Qian Liu[a], Haozhi Sha[a,g], Ke Bi[c], Ben Xu[a], Jing Ma[a], Lin Gu[f], Rong Yu[a,g], Yang Shen[a], Xiao Renshaw Wang[b,*], Judith L. MacManus-Driscoll[e], Chong-Lin Chen[a,h], Ce-Wen Nan[a], Yuan-Hua Lin[a,*]

[a]State Key Laboratory of New Ceramics and Fine Processing, School of Materials Science and Engineering, Tsinghua University, Beijing 100084, China
[b]Division of Physics and Applied Physics, School of Physical and Mathematical Sciences, Nanyang Technological University, Singapore 637371, Singapore
[c]State Key Laboratory of Information Photonics and Optical Communications, School of Science, Beijing University of Posts and Telecommunications, Beijing 100876, China
[d]MIIT Key Laboratory of Aerospace Information Materials and Physics, College of Science, Nanjing University of Aeronautics and Astronautics, Nanjing 211106, China
[e]Department of Materials Science and Metallurgy, University of Cambridge, 27 Charles Babbage Road, Cambridge CB3 0FS, United Kingdom
[f]Beijing National Laboratory for Condensed Matter Physics, Institute of Physics, Chinese Academy of Sciences, Beijing 100190, China
[g]National Centre for Electron Microscopy in Beijing, School of Materials Science and Engineering, Tsinghua University, Beijing 100084, China h Department of Physics and Astronomy, University of Texas at San Antonio, San Antonio, TX 78249, United States

Abstract

The presence of uncontrolled defects is a longstanding challenge for achieving high electric resistivity and high energy storage density in dielectric capacitors. In this study, opposite to conventional strategies to suppress defects, a new approach, i.e., constructing defects with deeper energy levels, is demonstrated to address the inferior resistivity of $BiFeO_3$-based dielectric films. Deep-level vacancy complexes with high charge carrier activation energies are realized via deliberate incorporation of oxygen vacancies and bismuth vacancies in low-oxygen-pressure deposited films. This method dramatically increases the resistivity by ~4 orders of magnitude and the breakdown strength by ~150%, leading to a ~460% enhancement of energy density (from 14 to 79 J cm^{-3}), as well as improved efficiency and performance reliability. This work reveals the significance of rational design and precise control of defects for high-performance dielectric energy storage. The deep-level vacancy complex approach is generalizable to wide ranges of dielectric systems and functional applications.

Keywords: dielectric energy storage, defect, vacancy complex, resistivity, energy density, $BiFeO_3$

1. Introduction

Dielectric capacitors with ultrafast charging-discharging speed are fundamental energy storage components in electronics and electrical power systems [1,2]. To realize device miniaturization, cost reduction and performance enhancement, dielectrics with high energy storage densities have been extensively pursued [3–6]. In the development of energy-storage dielectrics, material defect emerges as a longstanding obstacle [7,8]. Defects usually act as shallow charge carrier traps and severely degrade the electrical resistivity of dielectrics, which cause large leakage current, limit the breakdown strength, increase dielectric loss and destabilize dielectric polarization, consequentially deteriorating the energy density and operation reliability [9,10].

Fine control of defects, i.e., defect engineering, is thus highly demanded in dielectrics, yet the progress is rather limited compared with that in the semiconductor industry [11]. The challenges lie in the complexity of defects in dielectrics, for example, oxide dielectrics such as $PbTiO_3$ (PTO) and $BiFeO_3$ (BFO) contain complicated defect configurations including but not limited to cation vacancies, oxygen vacancy, ion valence variation, etc [12]. Moreover, the category, concentration and distribution of the defects can be sensitively altered by the specific composition, synthesis process and thermal history. These defects, even with a very low concentration, can make a remarkable impact on the electric properties of the insulating dielectrics. The widely used defect-engineering strategies in semiconductors, e.g., chemical doping to interact with or counteract existing defects, are less effective and sometimes act in contradictory ways in oxide dielectrics. For example, Ti doping in BFO in different studies separately reported increased and decreased resistivity [13,14], which was linked to the varied dominant defects in the pristine BFO, i.e., oxygen vacancies (V_O) [15,16] and bismuth vacancies

(V_{Bi}) [17,18] that result in *n*-type and *p*-type conduction, respectively. Therefore, more determinative defect engineering strategies are desirable to enhance the resistivity and energy storage performance of dielectrics.

Considering that the defects in oxide dielectrics are rather shallow in the bandgap (e.g, ~0.13 eV for V_{Bi} and ~0.60 eV for V_O) [19,20] but eliminating them is thermodynamically unpractical, transforming the shallow defects into deeper ones can be a feasible approach to reduce the charge carrier activation and to increase the resistivity. To this end, defect complexes that consist of inversely charged defects with electrostatic mutual attraction can be promising strategies. It has been reported that He^{2+} bombardment of oxide films such as BFO [21], PTO [22], and $Pb(Mg_{1/3}Nb_{2/3})O_3$-$PbTiO_3$ (PMN-PT) [4] can induce cation and oxygen vacancies simultaneously that form deep-energy-level defect complexes. For example, in the case of PTO films, $V_O^{\cdot\cdot} - V_{Pb}''$ and $V_O^{\cdot\cdot} - V_{Ti}'''' - V_O^{\cdot\cdot}$ with energy levels of ~1.0 eV were induced, while the shallow-level defects Pb^{3+} (~0.26 eV) and V_{Pb}'' (~0.56 eV) were suppressed. Thus, the films realize enhancements of resistivity by orders of magnitude [22].

In this work, we demonstrate a milder, less costly, yet efficient way to introduce defect complexes via in-situ control of the material fabrication, so as to improve the resistivity and energy storage performance of dielectrics. We employ the pulsed laser deposition (PLD) technique, in which multiple parameters can be precisely controlled to modulate the defects in deposited films [23–26]. By controlling the oxygen partial pressure (pO_2) during deposition, we construct $V_{Bi} - V_O$ defect complexes in BFO-based dielectric films. Contrary to the general perception that high pO_2 (>10^{-1} Torr) is favourable to suppress the V_O concentration and increase the resistivity of BFO, we deliberately utilize lower pO_2s at the level of 10^{-2} Torr to introduce both V_O and V_{Bi}, thus forming $V_{Bi} - V_O$ complexes with higher carrier activation

energies. The film resistivity is thus enhanced by ~4 orders of magnitude, which increases the breakdown strength by ~150% (to ~4 MV cm^{-1}) and thus breaks the bottleneck of BFO-based films for high-voltage dielectric energy storage. Ultimately, great enhancement of energy density from 14 to 79 J cm^{-3}, together with improved efficiency, performance reliability and thermal stability, is achieved in the optimized BFO-based dielectrics with $V_{Bi} - V_O$ complexes.

2. Results and discussion

BFO-based films were grown on (001)-oriented 0.7 wt% Nb-doped $SrTiO_3$ (Nb:STO) substrates with pO_2 varied from 50 to 5 mTorr. The composition of the films was designed as 30BFO-35$BaTiO_3$ (BTO)-35$SrTiO_3$ (STO) (denoted as BFBSTO) because it forms a relaxor ferroelectric (RFE) with unique polymorphic nanodomain structures and great energy storage potential [3]. All the BFBSTO films are high-quality epitaxial single-crystal perovskites, as affirmed by the results of scanning transmission electron microscopy (STEM, Fig. 1a) and X-ray diffraction (XRD, Fig. S1). With the decrease of pO_2, the films show a clear shift of the (002) XRD peak towards a smaller angle (Fig. 1b), corresponding to a *c*-axis lattice expansion from 3.96 to 4.03 Å. As the films have identical nominal compositions from the same PLD target, the lattice expansion is ascribed to ion vacancies induced during film deposition, which reduce the electrostatic constraint on the lattice [27]. In the BFBSTO films grown in reduced pO_2, more V_O should be introduced jointly by the BFO, BTO and STO components, in accordance with previous reports [15,28,29]. As for the possible cation vacancies, a reduction of the Bi/Fe ratio with decreased pO_2 is observed in the films via the inductively coupled plasma mass spectrometry (ICP-MS, Fig. 1c). The film composition transforms from slight Bi-excess (Bi/Fe ~1.15) at 50 mTorr to slight Bi-deficiency (Bi/Fe ~0.86) at 20 mTorr, and to strong Bi-deficiency (Bi/Fe ~0.59) at 5 mTorr. This evolution agrees with previous reports of PLD-fabricated BFO

films in which the Bi/Fe ratio was reduced from 1 to ~0.6 as pO_2 decreases to 1 mTorr [30]. Energy dispersive X-ray spectroscopy (EDS) shows a similar trend of Bi deficiency with lowered pO_2 in our films but a negligible variation of the (Ba+Sr)/Ti ratio near ~1.0 (Fig. S2a), which is ascribed to the much stronger volatility of the Bi than other elements. Therefore, V_{Bi} is introduced along with V_O during the low-pO_2 deposition, which can be understood from two aspects. For one thing, V_{Bi} is triggered to maintain charge compensation in the films, as expressed by $2Bi_{Bi} + 3O_O \rightarrow 2V_{Bi} + 3V_O + 2Bi\ (g) + \frac{3}{2}O_2$. For another, the lowered pO_2 during PLD leads to less scattering and higher kinetic energy of the adatoms arriving the substrate, which results in knock-on damage on the deposited films (similar to the ion bombardment) [22], facilitates the formation and alignment of defect complexes, and, thus, causes lattice expansion [31].

It is generally regarded that in ferrite or titanate materials, V_O donates electrons and induces valence reduction of neighbouring Fe and Ti atoms (Fe^{3+} to Fe^{2+}, and Ti^{4+} to Ti^{3+}) [28,32]. However, in our BFBSTO films, it is found that as the V_O concentration increases (with pO_2 lowered from 50 to 5 mTorr), the Fe^{2+} fraction does not increase but in fact decreases from 32% to 18% (Fig. 1c), while the Ti element valence remains +4, as demonstrated by X-ray photoelectron spectroscopy (XPS, Fig. 1d and Fig. S2b). This indicates that the V_O in the BFBSTO films is more likely to interact with V_{Bi}, forming $V_{Bi} - V_O$ defect complexes. Direct observation of defect complexes is so far technically not possible; yet their existence can be indirectly inferred from polarization-electric field (*P*-*E*) loops. Conventional RFE dielectrics present *P*-*E* loops with two d*P*/d*E* (differential of *P* regarding *E*) peaks, which correspond to the switching of polarization and FE domains. While in RFE dielectrics containing defect complexes, which are equivalent to dipoles consisting of positive and negative charges, FE

domains can be electrostatically pinned by the defect complexes [33]. This interaction, also called ageing, hinders the domain switching and causes pinched *P-E* loops with 4 peaks in the d*P*/d*E* curve [34]. The BFBSTO film grown under the pO_2 of 50 mTorr exhibits a normal *P-E* loop without pinching (Fig. S2), agreeing with the finding that it contains mainly V_O. For films grown under pO_2s of 20 and 5 mTorr, the *P-E* loops become pinched with 4 d*P*/d*E* peaks presented (Fig. 1e and Fig. S3), indicating the existence of $V_{Bi} - V_O$ complexes. Similar pinched *P-E* loops have also reported in pure BFO [35]. We notice that the pinch feature in our BFBSTO films is not as prominent as in pure BFO; this is because the nanodomains in the RFE BFBSTO are more dynamic and thus less strongly pinned by the defect complexes, compared with the ordinary FE domains in BFO.

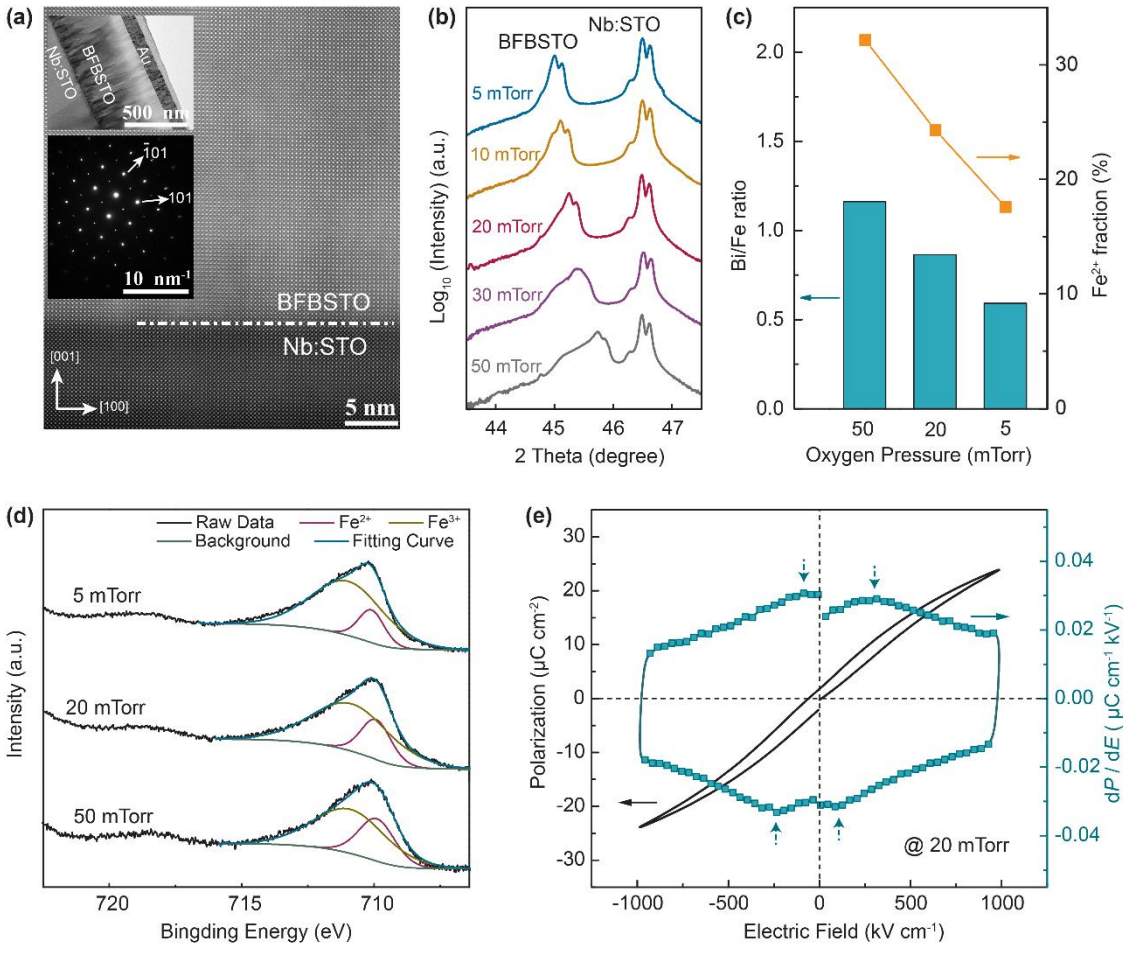

Fig. 1. (a) STEM atomic image of a BFBSTO film grown under a pO_2 of 20 mTorr. The insets are the low-magnification morphology of the film and the selected area electron diffraction at the BFBSTO/Nb:STO interface. (b) XRD patterns of the (002) diffraction peaks of BFBSTO films grown under varied pO_2s. (c) Evolution of the Bi/Fe ratio and the Fe^{2+} fraction with pO_2. (d) XPS spectra of Fe $2p_{3/2}$ peak and fitting of Fe valences. (e) Pinched *P*-*E* loop of the BFBSTO film with the pO_2 of 20 mTorr.

To understand the formation mechanism of the $V_{Bi} - V_O$ complex and its influence on electrical properties, we conducted first-principles calculations based on density functional theory. To simplify the calculation, the BTO and STO components were reasonably omitted, and a 2×2×2 supercell of BFO was employed (Fig. S4a). A Bi and an O atom were removed to simulate V_{Bi} and V_O, respectively. Details of the calculation can be found in the Experimental section. We first demonstrated that in all configurations of the $V_{Bi} - V_O$ complex, the nearest neighbouring configuration, with the smallest $V_{Bi} - V_O$ distance of 2.31 Å, has the lowest total energy (Fig. S4b). The electrostatic attraction between the vacancies is revealed to be the key driving force for the formation of the defect complexes [36]. This is evidenced by the negative association energy of the $V_{Bi} - V_O$ complex regardless of how its charge state (q) varies between +2 and -3 (Fig. S5). The largest association energy (-1.95 eV), corresponding to the strongest electrostatic force, is obtained when q = -1, i.e., the configuration with fully ionized vacancies $V_{Bi}''' - V_O^{\cdot\cdot}$. Moreover, we derived the energy levels (ϵ) and charge carrier activation energies (E_a) of the individual V_{Bi}, V_O, and the $V_{Bi} - V_O$ complex, from the calculated plots of

defect formation energies between the valence band maximum (VBM) and conduction band minimum (CBM) (Fig. 2). Here, ϵ_{VBM} is set as 0 eV and the ϵ_{CBM} of BFO (i.e., bandgap) is calculated to be 2.0 eV. For a defect *D* that transforms from q to q', the energy level $\epsilon_D(q/q')$ is given by the intersection of corresponding plots of formation energy. For example, $\epsilon_{V_O}(0/+1) = 1.37$ eV and $\epsilon_{V_{Bi}}(0/-1) = 0.12$ eV. The carrier activation energy $E_{\mathrm{a},D}(q/q')$ equals $\epsilon_{\mathrm{CBM}} - \epsilon_D(q/q')$ for donors and $\epsilon_D(q/q') - \epsilon_{\mathrm{VBM}}$ for acceptors, respectively. Therefore, the activation energies of the V_O donor $E_{\mathrm{a},V_O}(0/+1)$ and the V_{Bi} acceptor $E_{\mathrm{a},V_{Bi}}(0/-1)$ are 0.63 and 0.12 eV, respectively, in good agreement with previous theoretical calculations [36,37]. As for the $V_{Bi} - V_O$ complex, one can first notice that the q = -1 state possesses a much larger range of stability with the lowest forming energy compared with other states, in accordance with the largest association energy of the configuration $V_{Bi}''' - V_O^{\cdot\cdot}$. As a result, the activation energy levels of $V_{Bi}''' - V_O^{\cdot\cdot}$ are shifted deeper into the bandgap. More specifically, if $V_{Bi}''' - V_O^{\cdot\cdot}$ behaves as a donor, the activation energy should be $E_{\mathrm{a},V_{Bi}-V_O}(-1/0) = \epsilon_{\mathrm{VBM}} - \epsilon_{V_{Bi}-V_O}(-1/0) = 2.0 - 0.32$ eV = 1.68 eV, which is greatly enhanced compared with that of the individual V_O (0.63 eV). Similarly, considering it as an acceptor, $E_{\mathrm{a},V_{Bi}-V_O}(-1/-2) = \epsilon_{V_{Bi}-V_O}(-1/-2) - \epsilon_{\mathrm{VBM}}$ = 1.65 eV, which is also much larger than that of the individual V_{Bi} (0.12 eV). Therefore, the activation of both electron and hole carriers are greatly suppressed by the $V_{Bi} - V_O$ vacancy complex, which can significantly improve the resistivity of BFO-based materials.

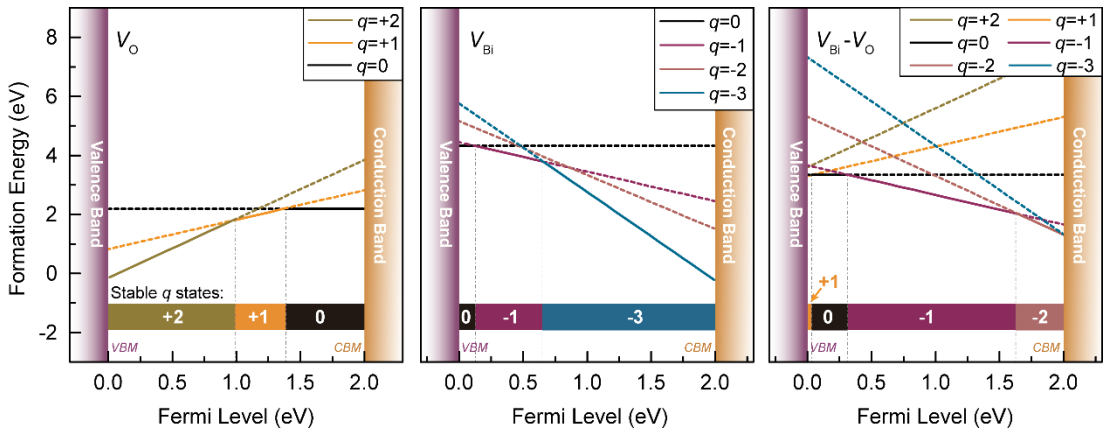

Fig. 2. First-principles calculations of the formation energies of V_O, V_{Bi} and $V_{Bi} - V_O$ defects as a function of the Fermi level for different charge states. The solid lines indicate the charge state q with the lowest formation energy, i.e., the highest stability, while the dash lines indicate states with higher formation energy and lower stability. The stable ranges of the defect charge state q between VBM and CBM are displayed.

To experimentally characterize the enhancement of resistivity by $V_{Bi} - V_O$ complexes, impedance spectra of the BFBSTO films were measured, as shown in Fig. 3a-c. The insets show the fine spectrum structures at the high frequency (ω) range. All the spectra can be fitted with two in-series R-CPE units (inset of Fig. 3b), with each R-CPE unit consisting of an ideal resistor (R) and a constant-phase element (CPE) connected in parallel. Because the films are single crystalline, the effect of grain boundaries is negligible. The lower-ω semi-circle in the impedance plots is ascribed to the film-electrode interfaces, and the higher-ω one to the grains in the film [38]. For the 50-mTorr film at 623 K (Fig. 3a), the fitted interfacial resistivity R1 and grain resistivity R2 are 60.5 and 2.9 kΩ m, respectively, indicating that the interfaces are the main

contributors to the film resistivity, while the grains are much less resistive due to the existence of V_O. This result agrees well with previous observations in BFO films [38]. The reciprocals of R1 and R2 (i.e., conductivity σ) are fitted regarding the temperature based on the Arrhenius law (Fig. 3d). The activation energies E_a for the interface and grain conductivity are 0.94 and 0.88 eV, respectively, consistent with the reported values of V_O [39,40]. For the 20-mTorr film, R1 and R2 increase remarkably to 308.9 and 58.2 kΩ m (Fig. 3b), which are 5 and 20 times the values of the 50-mTorr film, respectively. Besides, E_a of the interface and grain conductivity increases to 1.10 and 1.04 eV, respectively (Fig. 3e). The impedance becomes jointly contributed from the grain and interface in the 20-mTorr film. This is because of the formation of $V_{Bi} - V_O$ complexes, which, for one thing, greatly increases the grain resistivity by compensating V_O and suppressing charge activation; and for another, improves the interface resistivity possibly by reducing the accumulation of oxygen vacancy near the interfaces and increasing the Schottky barrier height [41]. As the pO$_2$ further reduces to 5 mTorr (Fig. 3c), the resistivity is again degraded (R1 = 68.4 and R2 = 1.3 kΩ m), and the activation energies also decrease to 0.84 and 0.62 eV, respectively (Fig. 3f). We propose that there is an upper limit for the stable formation of $V_{Bi} - V_O$ complexes. The excessive V_O defect induced by the excessively low pO$_2$ become uncompensated, which decreases the resistivity. This proposition is supported by the enhanced resistivity of the 5-mTorr BFBSTO film after further annealing in high-pressure O$_2$ (Fig. S6).

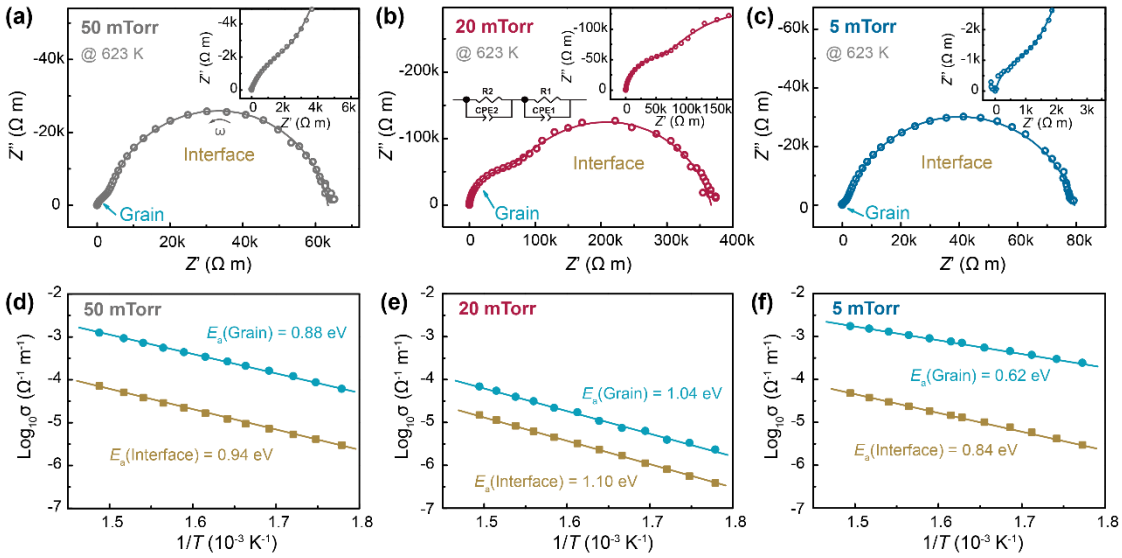

Fig. 3. Impedance spectra and conduction activation energy fitting of BFBSTO films. Complex impedance (*Z*' - *Z*'') spectra measured at 623 K for films grown under pO_2s of (a) 50 mTorr, (b) 20 mTorr, and (c) 5 mTorr. The insets show the fine spectrum structures in the high frequency range. The circles are experimental results, and the lines are fitting results based on the equivalent circuit with two R-CPE units in-series (inset of Fig. 3b). Fittings of the interface and grain conduction regarding the temperature *T* of BFBSTO films with pO_2s of (d) 50 mTorr, (e) 20 mTorr and (f) 5 mTorr.

The DC leakage current of the BFBSTO films was also measured (Fig. 4a), whose evolution agrees with the impedance spectra. At an electric field of 1 MV cm^{-1}, the 50-mTorr film shows a high leakage current of 2×10^{-2} A cm^{-2}, comparable with those of previously reported BFO-based films [42]. As the pO_2 decreases to 20 mTorr, the leakage current is distinctly suppressed by almost 4 orders of magnitude. The ultralow current density of 5×10^{-6} A cm^{-2} (at 1 MV cm^{-1}) reaches the lowest level of perovskite dielectric films, which demonstrates the effectiveness of

$V_{Bi} - V_O$ complexes in improving the resistivity. With the pO$_2$ further reducing to 5 mTorr, the leakage current increases again to 3×10^{-3} A cm^{-2} due to the excess V_O. Mechanisms of the leakage currents were also analysed (Fig. S7). At lower fields, the 20-mTorr film follows Ohm's law, while the 50- and 5-mTorr films exhibit space-charge-limited conduction, which is ascribed to charge carriers from V_O. At higher fields, the leakage current of the 50- and 5-mTorr films is dominated by the interfacial Schottky emission. While in the 20-mTorr film, interfacial Schottky emission and bulk Poole-Frenkel emission take effect jointly [43]. These phenomena match well with the impedance spectra (Fig. 3), indicating that $V_{Bi} - V_O$ complex increases both the grain and interface resistivity. In addition, in BFO-based films of other compositions we observed similar trends of leakage current with pO$_2$ (Fig. S8). In 40BFO-60STO films, the lowest leakage current is realized at a pO$_2$ of 10 mTorr; while in 25BFO-75BTO films, the best pO$_2$ is 25 mTorr. These results prove that the construction of deep $V_{Bi} - V_O$ complexes in the optimized pO$_2$ is a universal technique for resistivity enhancement in BFO-based films.

Since low resistivity is known to deteriorate both electrical and thermal breakdown of dielectrics [44], it is not surprising that the 50-mTorr film exhibits a low characteristic breakdown field E_b of only 1.6 MV cm^{-1}, as derived from the two-parameter Weibull distribution (Fig. 4b). With the improvement of resistivity by vacancy complexes, the 20-mTorr film exhibits a remarkable enhancement of E_b by 150%, reaching a maximum value of 4.0 MV cm^{-1}. This value is comparable with those of other insulating perovskite dielectric films, e.g., PZT and BZT [45,46]. The great improvements of resistivity and breakdown field overcome the bottleneck of BFO-based dielectrics for high-voltage energy storage applications.

Because dielectric energy storage is closely linked to not only the breakdown strength but also the dielectric polarization (see schematic in Fig. S9), we investigated the dielectric

properties of the BFBSTO films. As shown in Fig. 4c, the dielectric permittivity decreases from 293 to 205 (at 1 kHz) as the pO_2 decreases. This can be ascribed to the increased Bi deficiency, as the Bi $6s^2$ lone electron pair is one of the main contributors to the ferroelectric polarization of BFO [47]. The 50-mTorr and 5-mTorr films exhibit high dielectric loss at low frequencies, e.g., 0.23 and 0.07 at 100 Hz, respectively, which originates from the V_O-related space charge [44]. The 20-mTorr film with $V_{Bi} - V_O$ complexes greatly suppresses the space charge and thus exhibits a loss tangent of as low as 0.02, which reaches the best level of perovskite dielectric films [45]. The temperature dependence of the dielectric properties was also shown in Fig. S10. The 50- and 5-mTorr films exhibit remarkable elevation of permittivity and deterioration of loss tangent with increased temperature, which is ascribed to the thermal activation of the V_O-related space charges. As comparison, the 20-mTorr film maintains stable permittivity and low loss tangent at temperatures even up to 480 K, benefitting from the large activation energy of the $V_{Bi} - V_O$ complexes.

Fig. 4d exhibits the polarization behaviours of the BFBSTO films. A drop of the maximum polarization (P_m) from 41 to 25 μC cm^{-2} at the electric field of 1.5 MV cm^{-1} is observed, associated with the Bi deficiency at lower pO_2s. The ferroelectric nonlinearity is also weakened: the *P-E* loop of the 5-mTorr film becomes similar to a paraelectric compared with that of the 50-mTorr film. The remnant polarization (P_r, inset of Fig. 4d) shows a similar trend as the low-frequency dielectric loss (Fig. 3c) and the leakage current (Fig. 4a). This is reasonable as P_r is contributed by both the ferroelectric loss and conduction loss [32]. The portion of P_r from the ferroelectric loss is characterized by the positive-up-negative-down (PUND) technique (Fig. S11 and Table S1), which shows a monotonous decrease with pO_2 (inset of Fig. 4d), again proving the depression of ferroelectricity by Bi deficiency. The other part of P_r from conduction loss can

then be obtained, which is minimal in the 20-mTorr film but visible in the 50- and 5-mTorr films. These observations suggest that the formation of $V_{Bi} - V_O$ complex is at the slight sacrifice of polarization. This is, however, a worthwhile compromise as the dielectric loss and P_r are greatly suppressed, which is critical for high-performance energy storage.

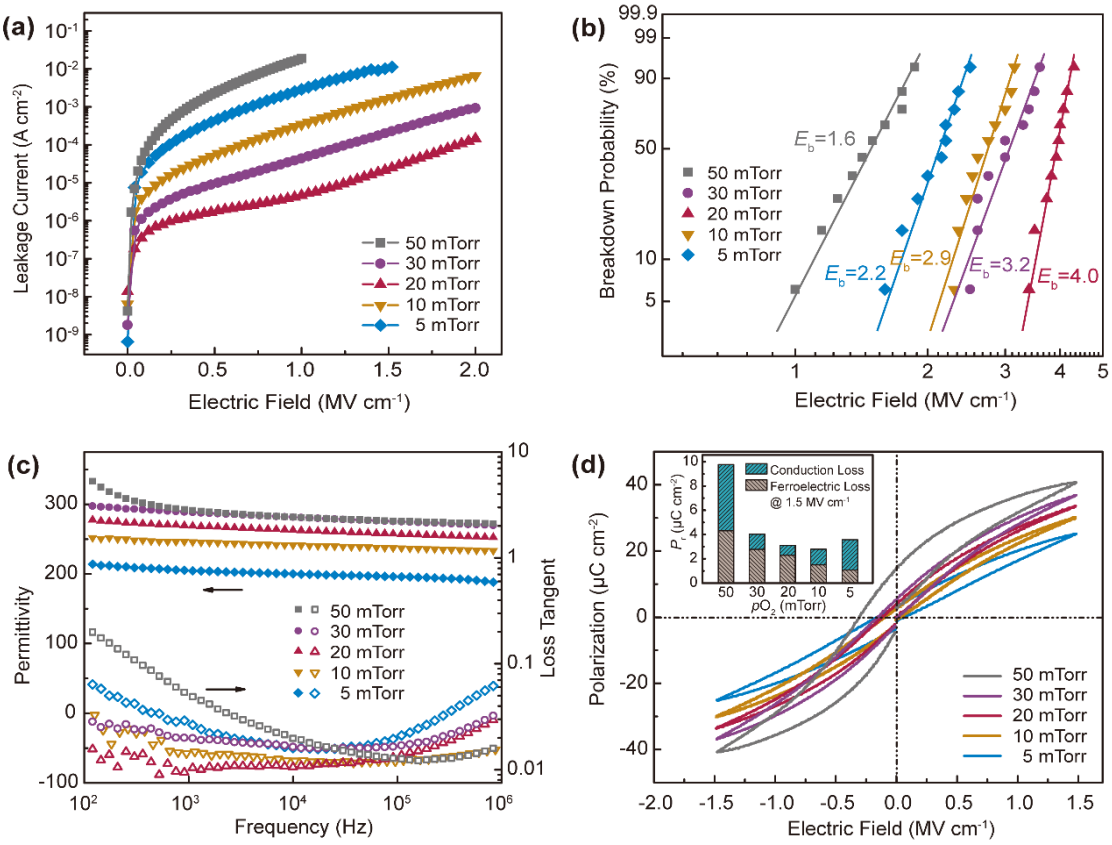

Fig. 4. Electric and dielectric properties of BFBSTO films. (a) Leakage current density as a function of biased DC electric field. (b) Two-parameter Weibull distribution analysis of the breakdown strength. (c) Frequency-dependent dielectric permittivity and loss tangent; (d) *P-E* loops. The inset shows the P_r contributed by ferroelectric loss and conduction loss of the BFBSTO films.

To obtain the energy storage performance, we measured the *P-E* loops of the BFBSTO films at fields up to E_b (Fig. S12). The energy density U_e and efficiency η are calculated based on the equations $U_e = \int_{P_r}^{P_m} PdE$ and $\eta = U_e/(U_e+U_{loss})$ (Fig. S9), where U_{loss} is the hysteresis energy loss (including ferroelectric loss and conduction loss) in the charging-discharging cycle. The results are displayed in Fig. 5a. At the same field of 1.5 MV cm^{-1}, the 20-mTorr film exhibits an optimally suppressed conduction loss, and thus realizes greatly enhanced U_e of 20 J cm^{-3} and η of 87% compared with other films (e.g., U_e of 13 J cm^{-3} and η of 53% in the 50-mTorr film). Moreover, the enhanced E_b enabled by resistivity improvement further raises the ceiling of energy storage capability for the 20-mTorr film, which realizes an ultrahigh U_e of 79 J cm^{-3} at the E_b of 4.0 MV cm^{-1}, representing a 4.6-time enhancement compared with the 50-mTorr film (14 J cm^{-3} at the E_b of 1.6 MV cm^{-1}). In addition, while other films experience a sharp decline of η due to the deteriorated U_{loss} at high *E*, a high η of >78% is maintained in the 20-mTorr film. These enhancements in energy storage performance clearly demonstrate the significance of improved resistivity by vacancy complexes. A comparison of the energy performance of our BFBSTO film with representative BTO-based, PTO-based and other BFO-based films is shown in Fig. 5b [45,48–58]. Note that the growth trend of U_e with *E* in BFO-based films is at the same level as PTO-based films and is more rapid than that of BTO-based films. This is because the spontaneous polarization of BFO (~90 μC cm^{-2}) is comparable with that of PTO (78 μC cm^{-2}) and is much larger than that of BTO (26 μC cm^{-2}), rendering BFO-based films promising as Pb-free energy-storage dielectrics. The vacancy complex strategy in this work breaks the limitations of low resistivity and small E_b of BFO-based films, making their U_e competitive with Pb-based films. Furthermore, the vacancy complex strategy also facilitates the breach of the

adverse coupling between U_e and η, realizing concurrent optimization and making the BFO-based dielectric films even more outstanding for practical utilization (Fig. 5b).

The performance reliability with respect to the charging-discharging cycles and working temperatures was also characterized. The 20-mTorr BFBSTO film undergoes a charging-discharging process over 1×10^8 cycles at an electric field of 2.2 MV cm^{-1} with negligible degradation of energy performance (Fig. 5c and Fig. S13). This should be ascribed to the RFE nanodomain structures of BFBSTO that suppress domain pinning and polarization fatigue [3]. Besides, the high resistivity and high E_b of the 20-mTorr film prevents failure during the cycles, which happens easily in the 5-mTorr and 50-mTorr films. The energy storage performance of the BFBSTO films between -100 and 150 ^oC is also presented (Fig. 5d and Fig. S14). The 20-mTorr film shows stable U_e and η, with variations of <4% and <10%, respectively, over the whole temperature range. This excellent stability is first due to the RFE nature of BFBSTO films that realizes thermally stable dielectric and polarization behaviours. More importantly, the $V_{Bi} - V_O$ complexes strongly trap charge carriers, reduce carrier activation, and mitigate the conduction loss at high temperatures. This is in stark contrast to the films of 50 and 5 mTorr, in which the leakage current increases dramatically with temperature (Fig. S15), resulting in distorted *P-E* loops and degenerated energy storage performance [59].

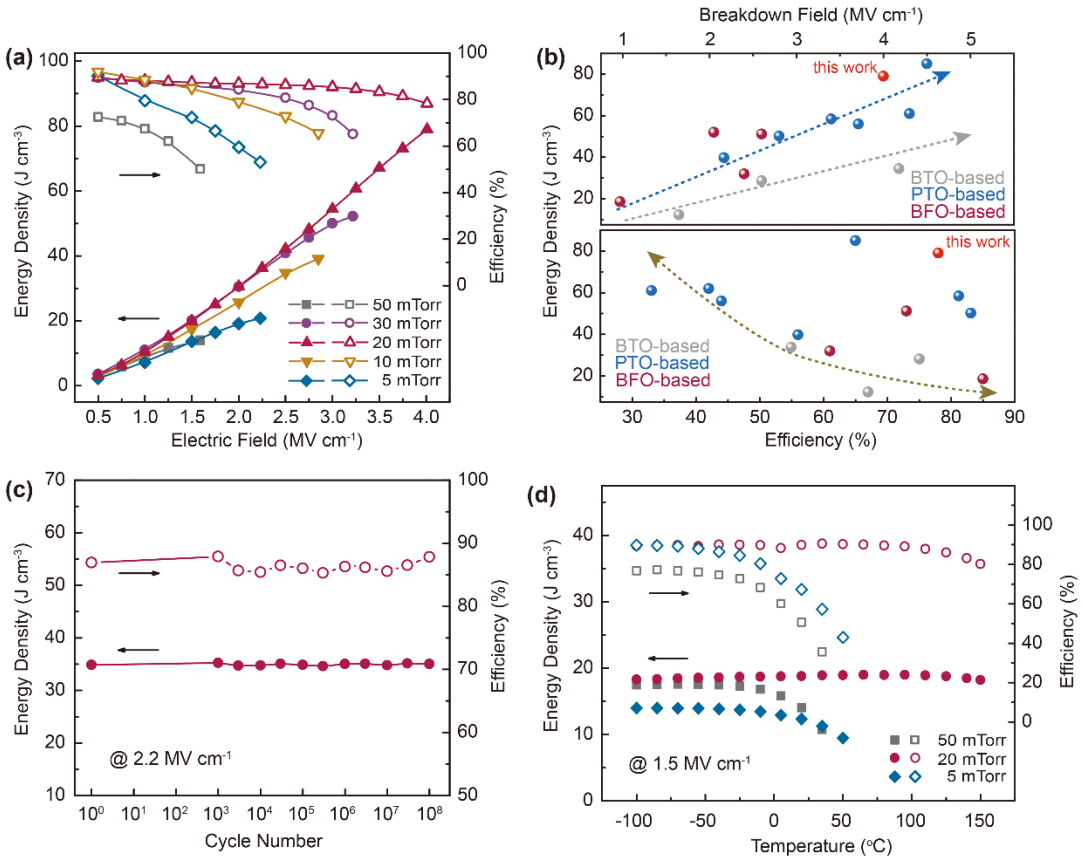

Fig. 5. Dielectric energy storage performance of the BFBSTO films. (a) Energy density and efficiency of the films as functions of the electric field; (b) Comparison of energy storage performance of the BFBSTO film in this work with representative PTO-based, BTO-based, and other BFO-based dielectric films; (c) Energy storage performance of the 20-mTorr BFBSTO film at an electric field of 2.2 MV cm^{-1} over 10^8 charging-discharging cycles; (d) Temperature dependence of the energy storage performance of the BFBSTO films at a field of 1.5 MV cm^{-1}.

3. Conclusions

To conclude, we demonstrate an effective approach of constructing deep-level $V_{Bi} - V_O$ complexes to enhance the resistivity and dielectric energy storage performance of BFO-based

films. The $V_{Bi} - V_O$ complexes are realized by deliberately introducing both O and Bi deficiencies with a low pO$_2$ during film deposition. The charge carrier activation energies are greatly enhanced by the $V_{Bi} - V_O$ complexes, as revealed by theoretical calculations and experimental characterizations. The film resistivity is thus improved by ~4 orders of magnitude, which reduces the dielectric loss to as low as 0.02, improves the breakdown strength to 4.0 MV cm^{-1} and thus gives rise to a ~460% enhancement of energy density (from 14 to 79 J cm^{-3}). Improved energy storage efficiency and operational reliability are also achieved. The vacancy complex offers a new, feasible and effective approach to address the longstanding bottleneck, i.e., inferior resistivity of BFO-based materials for high-voltage dielectric applications. This work could be a paradigm applicable for a wide range of materials (Pb-based, Bi-based, Na/K-based, *etc.*) in which vacancy complexes have a high possibility to form and to exert influence on dielectric and other functional properties.

4. Experimental section

4.1 Film Preparation

BFBSTO ceramic target was prepared with cold isostatic pressing and sintered by conventional solid-state reaction at 1100 ^{o}C for 2h. To compensate for the Bi volatilization during sintering, 15 mol% Bi was added in excess. The BFBSTO films were deposited in a PLD system with a KrF excimer laser. The laser wavelength was 248 nm, the repetition rate was 10 Hz and the laser energy was ~1.5 J cm^{-2}. (001)-oriented 0.7wt% Nb-doped $SrTiO_3$ (Nb:STO) single crystals were used as substrates and served as the bottom electrodes. The substrate temperature was kept at 700 ^{o}C during deposition. The BFBSTO films were grown under varied pO$_2$ in the range of 50 - 5 mTorr. After deposition, the films were in-situ annealed in 500 Torr O_2 for 30 min at 500 ^{o}C to reduce excess oxygen deficiency and then cooled down at a rate of 10 ^{o}C min^{-1}. The film thicknesses were ~500 nm, as confirmed by scanning electron microscopy (SEM,

Merlin, Zeiss). Circular Au top electrodes (~300 μm in diameter and ~100 nm in thickness) were sputtered for electrical measurements.

4.2 Characterizations

Film crystal structure and epitaxial properties were characterized using an X-ray diffractometer (XRD; Smartlab, Rigaku) with Cu K_α radiation (λ = 1.5418 Å). The cross-sectional low-magnitude morphology and high-magnitude atomic images were obtained with the high-resolution scanning transmission electron microscopy (STEM; JEOL ARM200CF). The film composition was measured with inductively coupled plasma mass spectrometry (ICP-MS; iCAP Q, Thermo Fisher Scientific). X-ray photoelectron spectroscopy (XPS) was collected using a SPECS PHOIBOS 150 electron energy analyzer. Impedance properties were studied using an electrochemical impedance Spectroscopy (Solartron 1260 and 1278) with an AC voltage of 100 mV, in the frequency range of 1 Hz to 5 MHz and temperature range of 543 to 623 K. The temperature was controlled by a home-made heating system. The dielectric permittivity and loss tangent were obtained with HP 4294A (Agilent) and LCR-8105G (GW Instek) with a perturbation AC voltage of 500 mV. The ferroelectric and leakage current properties were measured with Precision Multiferroic II (Radiant Technologies). Bipolar and unipolar *P-E* loops were collected with 1 kHz triangular voltage waves. The leakage currents were obtained with a series of DC voltages, with 200-ms soak time and 200-ms measure time for each voltage.

4.3. First-principles Calculations

The first-principles calculations were based on density functional theory (DFT) within the local density approximation (LDA) for exchange-correlation potential as implemented in Vienna *Ab initio* Simulation Package (VASP). The onsite Coulomb interaction was included in the LDA+*U* approach with a Hubbard parameter U_{eff} = 4 eV for Fe 3*d* electrons. Projector augmented wave methods (PAW) were used to describe the electron-ion interaction with Bi($5d^{10}6s^26p^3$), Fe($3p^63d^64s^2$) and O($2s^22p^4$). A periodic *R*3*c* structure of a 2×2×2 BFO supercell was employed with G-type antiferromagnetic order, as shown in Fig. S4. We simulated single Bi, O vacancies and Bi-O vacancy complex with different charge states. All defective supercells were relaxed while keeping the lattice parameters fixed at the perfect rhombohedral BFO values.

The plane-wave cutoff was set at 500 eV and the Brillouin Zone was sampled with a 3×3×3 *k*-point mesh. All atoms wer allowed to move until the Hellmann-Feynman force on each atom was smaller than 0.01 eV/Å and the total energy was converged to 10^{-5} eV. To determine the most stable Bi-O divacancy structure, seven configurations with different Bi-O divacancy distances were modelled. The nearest neighboring configuration was revealed to possess the lowest DFT total energy (Fig. S4), which was thus adopted in the following calculations.

The formation energy of defect *D* with charge state *q* was calculated as follows:

$$E_f(D,q) = E(D,q) - E(perfect) + \sum_i \mu_i + q(E_F + E_{VBM}) \quad (1)$$

where *E*(*D*, *q*) and *E*(perfect) were the DFT total energies of the defective and perfect supercells, respectively. The chemical potentials μ_i of the removed atoms were related by $\mu_i = \mu_i^0 + \Delta\mu_i$, where μ_i^0 was the chemical potential of the elemental solid and $\Delta\mu_i$ was determined by the thermodynamical constrains. The Fermi level E_F was defined relative to the valence band maximum (E_{VBM}) and could vary from zero up to the band gap of BFO. E_{VBM} was described as $E_{VBM} = E(perfect) - E(perfect + 1)$, with $E(perfect + 1)$ being the energy of a perfect supercell in which an electron had been removed. For charged defects, a neutralizing background charge was applied, and their energies were corrected by the monopole part of Makov-Payne and by the band alignment onto the perfect supercell with the shift of the orbital energy of the semi-core Fe 3*s* state [36]. Based on Eqn. (1), the association energy of the $V_{Bi} - V_O$ complex with various charge states was obtained:

$$E_{assoc}(V_{Bi} - V_O, q_1 + q_2) = E_f(V_{Bi} - V_O, q_1 + q_2) - E_f(V_{Bi}, q_1) - E_f(V_O, q_2) \quad (2)$$

Where q_1 and q_2 are the charge state of $V_{Bi}$and V_O, respectively. The results are shown in Fig. S5. The transition energy level $\epsilon(q/q')$ representing the energy required to ionize a defect with charge state q to another charge state q' was given by

$$\epsilon_D(q/q') = \frac{E_f(D,q) - E_f(D,q')}{q' - q} \quad (3)$$

4.4. Weibull Distribution Analysis

The characterized dielectric breakdown strength E_b of the samples was obtained with a two-parameter Weibull distribution function:

$$P(E) = 1 - \exp\left(-\left(E / E_b\right)^{\beta}\right) \quad (4)$$

where E is the measurement breakdown field, $P(E)$ is the cumulative probability of electric breakdown at E. When E equals E_b, $P(E)$ equals 63.2%. The Weibull parameter β evaluates the distribution of E. In this work, the breakdown field data of 10 samples for each pO_2 were collected for the fitting.

Declaration of competing interest

The authors declare no conflict of interest.

Acknowledgments

We thank Prof. Renchao Che, Dr. Mengfan Guo, Mr. Ke Pei, and Mr. XY Tan for fruitful discussions. This work was supported by the Natural Science Foundation of China (NSFC) via the Basic Science Center Project grant 51788104, NSFC grants 51532003, 51790490, 52072209 and 1729201. X.R.W. acknowledges supports from the Singapore National Research Foundation (NRF) under the Competitive Research Programs (CRP Grant No. NRF-CRP21-2018-0003). J.L.M-D. would like to thank the Royal Academy of Engineering grant CIET 1819_24.

Appendix A. Supplementary material

Supplementary data associated with this article can be found in the online version.

References

[1] B. Chu, X. Zhou, K. Ren, B. Neese, M. Lin, Q. Wang, F. Bauer, Q.M. Zhang, A dielectric polymer with high electric energy density and fast discharge speed, Science (80-.). 313 (2006) 334–336. https://doi.org/10.1126/science.1127798.

[2] Q. Li, L. Chen, M.R. Gadinski, S. Zhang, G. Zhang, H. Li, A. Haque, L.Q. Chen, T. Jackson, Q. Wang, Flexible higherature dielectric materials from polymer nanocomposites, Nature. 523 (2015) 576–579. https://doi.org/10.1038/nature14647.

[3] H. Pan, F. Li, Y. Liu, Q. Zhang, M. Wang, S. Lan, Y. Zheng, J. Ma, L. Gu, Y. Shen, P. Yu, S. Zhang, L.Q. Chen, Y.H. Lin, C.W. Nan, Ultrahigh–energy density lead-free dielectric films via polymorphic nanodomain design, Science (80-.). 365 (2019) 578–582. https://doi.org/10.1126/science.aaw8109.

[4] J. Kim, S. Saremi, M. Acharya, G. Velarde, E. Parsonnet, P. Donahue, A. Qualls, D. Garcia, L.W. Martin, Ultrahigh capacitive energy density in ion-bombarded relaxor ferroelectric films, Science (80-.). 369 (2020) 81–84. https://doi.org/10.1126/science.abb0631.

[5] J. Jiang, Z. Shen, J. Qian, Z. Dan, M. Guo, Y. Lin, C.W. Nan, L. Chen, Y. Shen, Ultrahigh discharge efficiency in multilayered polymer nanocomposites of high energy density, Energy Storage Mater. 18 (2019) 213–221. https://doi.org/10.1016/j.ensm.2018.09.013.

[6] M.D. Nguyen, E.P. Houwman, M.T. Do, G. Rijnders, Relaxor-ferroelectric thin film heterostructure with large imprint for high energy-storage performance at low operating voltage, Energy Storage Mater. 25 (2020) 193–201. https://doi.org/10.1016/j.ensm.2019.10.015.

[7] H.L. Tuller, S.R. Bishop, Point defects in oxides: Tailoring materials through defect engineering, Annu. Rev. Mater. Res. 41 (2011) 369–398. https://doi.org/10.1146/annurev-matsci-062910-100442.

[8] Y. Feng, J. Wu, Q. Chi, W. Li, Y. Yu, W. Fei, Defects and Aliovalent Doping Engineering in Electroceramics, Chem. Rev. 120 (2020) 1710–1787. https://doi.org/10.1021/acs.chemrev.9b00507.

[9] H. Palneedi, M. Peddigari, G.T. Hwang, D.Y. Jeong, J. Ryu, High-Performance Dielectric Ceramic Films for Energy Storage Capacitors: Progress and Outlook, Adv. Funct. Mater. 28 (2018) 1803665. https://doi.org/10.1002/adfm.201803665.

[10] L. Yang, X. Kong, F. Li, H. Hao, Z. Cheng, H. Liu, J.F. Li, S. Zhang, Perovskite lead-free dielectrics for energy storage applications, Prog. Mater. Sci. 102 (2019) 72–108. https://doi.org/10.1016/j.pmatsci.2018.12.005.

[11] E.G. Seebauer, K.W. Noh, Trends in semiconductor defect engineering at the nanoscale, Mater. Sci. Eng. R Reports. 70 (2010) 151–168. https://doi.org/10.1016/j.mser.2010.06.007.

[12] J.L. MacManus-Driscoll, M.P. Wells, C. Yun, J.W. Lee, C.B. Eom, D.G. Schlom, New approaches for achieving more perfect transition metal oxide thin films, APL Mater. 8 (2020) 40904. https://doi.org/10.1063/5.0003268.

[13] X. Qi, J. Dho, R. Tomov, M.G. Blamire, J.L. MacManus-Driscoll, Greatly reduced leakage current and conduction mechanism in aliovalent-ion-doped BiFeO3, Appl. Phys. Lett. 86 (2005) 1–3. https://doi.org/10.1063/1.1862336.

[14] G.D. Hu, S.H. Fan, C.H. Yang, W.B. Wu, Low leakage current and enhanced ferroelectric properties of Ti and Zn codoped BiFe O3 thin film, Appl. Phys. Lett. 92 (2008) 192905. https://doi.org/10.1063/1.2918130.

[15] J. Seidel, P. Maksymovych, Y. Batra, A. Katan, S.Y. Yang, Q. He, A.P. Baddorf, S. V. Kalinin, C.H. Yang, J.C. Yang, Y.H. Chu, E.K.H. Salje, H. Wormeester, M. Salmeron, R. Ramesh, Domain wall conductivity in La-doped BiFeO3, Phys. Rev. Lett. 105 (2010) 197603. https://doi.org/10.1103/PhysRevLett.105.197603.

[16] G.W. Pabst, L.W. Martin, Y.H. Chu, R. Ramesh, Leakage mechanisms in BiFe O3 thin films, Appl. Phys. Lett. 90 (2007) 72902. https://doi.org/10.1063/1.2535663.

[17] T. Rojac, A. Bencan, G. Drazic, N. Sakamoto, H. Ursic, B. Jancar, G. Tavcar, M. Makarovic, J. Walker, B. Malic, D. Damjanovic, Domain-wall conduction in ferroelectric BiFeO 3 controlled by accumulation of charged defects, Nat. Mater. 16 (2017) 322–327. https://doi.org/10.1038/nmat4799.

[18] A. Chen, W. Zhang, L.R. Dedon, D. Chen, F. Khatkhatay, J.L. MacManus-Driscoll, H. Wang, D. Yarotski, J. Chen, X. Gao, L.W. Martin, A. Roelofs, Q. Jia, Couplings of Polarization with Interfacial Deep Trap and Schottky Interface Controlled Ferroelectric Memristive Switching, Adv. Funct. Mater. 30 (2020) 2000664. https://doi.org/10.1002/adfm.202000664.

[19] Z. Zhang, P. Wu, L. Chen, J. Wang, Density functional theory plus U study of vacancy formations in bismuth ferrite, Appl. Phys. Lett. 96 (2010) 232906. https://doi.org/10.1063/1.3447369.

[20] S.J. Clark, J. Robertson, Energy levels of oxygen vacancies in BiFeO3by screened exchange, Appl. Phys. Lett. 94 (2009) 22902. https://doi.org/10.1063/1.3070532.

[21] S. Saremi, R. Xu, L.R. Dedon, R. Gao, A. Ghosh, A. Dasgupta, L.W. Martin, Electronic Transport and Ferroelectric Switching in Ion-Bombarded, Defect-Engineered BiFeO3 Thin Films, Adv. Mater. Interfaces. 5 (2018) 1700991. https://doi.org/10.1002/admi.201700991.

[22] S. Saremi, R. Xu, L.R. Dedon, J.A. Mundy, S.L. Hsu, Z. Chen, A.R. Damodaran, S.P. Chapman, J.T. Evans, L.W. Martin, Enhanced Electrical Resistivity and Properties via Ion Bombardment of Ferroelectric Thin Films, Adv. Mater. 28 (2016) 10750–10756. https://doi.org/10.1002/adma.201603968.

[23] A. Tsurumaki, H. Yamada, A. Sawa, Impact of Bi deficiencies on ferroelectric resistive switching characteristics observed at p-type schottky-like Pt/Bi 1-δFeO 3 interfaces, Adv. Funct. Mater. 22 (2012) 1040–1047. https://doi.org/10.1002/adfm.201102883.

[24] S.A. Lee, H. Jeong, S. Woo, J.Y. Hwang, S.Y. Choi, S.D. Kim, M. Choi, S. Roh, H. Yu, J. Hwang, S.W. Kim, W.S. Choi, Erratum: Phase transitions via selective elemental vacancy engineering in complex oxide thin films (Scientific Reports (2016) 6 (23649) DOI: 10.1038/srep23649), Sci. Rep. 6 (2016) 23649. https://doi.org/10.1038/srep24695.

[25] L.R. Dedon, S. Saremi, Z. Chen, A.R. Damodaran, B.A. Apgar, R. Gao, L.W. Martin, Nonstoichiometry, Structure, and Properties of BiFeO3 Films, Chem. Mater. 28 (2016) 5952–5961. https://doi.org/10.1021/acs.chemmater.6b02542.

[26] A. Kursumovic, W.W. Li, S. Cho, P.J. Curran, D.H.L. Tjhe, J.L. MacManus-Driscoll, Lead-free relaxor thin films with huge energy density and low loss for high temperature applications, Nano Energy. 71 (2020) 104536. https://doi.org/10.1016/j.nanoen.2020.104536.

[27] A. Dasgupta, S. Saremi, X. Ruijuan, L.R. Dedon, S. Pandya, A.R. Damodaran, L.W. Martin, Nonstoichiometry, structure, and properties of Ba1-xTiOy thin films, J. Mater. Chem. C. 6 (2018) 10751–10759. https://doi.org/10.1039/c8tc02725k.

[28] D.A. Muller, N. Nakagawa, A. Ohtomo, J.L. Grazul, H.Y. Hwang, Atomic-scale imaging of nanoengineered oxygen vacancy profiles in SrTiO3, Nature. 430 (2004) 657–661. https://doi.org/10.1038/nature02756.

[29] Y. Shuai, S. Zhou, D. Bürger, H. Reuther, I. Skorupa, V. John, M. Helm, H. Schmidt, Decisive role of oxygen vacancy in ferroelectric versus ferromagnetic Mn-doped BaTiO3 thin films, J. Appl. Phys. 109 (2011) 084105. https://doi.org/10.1063/1.3576125.

[30] L. You, N.T. Chua, K. Yao, L. Chen, J. Wang, Influence of oxygen pressure on the ferroelectric properties of epitaxial BiFeO3 thin films by pulsed laser deposition, Phys. Rev. B - Condens. Matter Mater. Phys. 80 (2009) 24105. https://doi.org/10.1103/PhysRevB.80.024105.

[31] A.R. Damodaran, E. Breckenfeld, Z. Chen, S. Lee, L.W. Martin, Enhancement of Ferroelectric Curie Temperature in BaTiO3 Films via Strain-Induced Defect Dipole Alignment, Adv. Mater. 26 (2014) 6341–6347. https://doi.org/10.1002/adma.201400254.

[32] H. Pan, J. Ma, J. Ma, Q. Zhang, X. Liu, B. Guan, L. Gu, X. Zhang, Y.J. Zhang, L. Li, Y. Shen, Y.H. Lin, C.W. Nan, Giant energy density and high efficiency achieved in bismuth ferrite-based film capacitors via domain engineering, Nat. Commun. 9 (2018) 1813. https://doi.org/10.1038/s41467-018-04189-6.

[33] H. Pan, A. Kursumovic, Y.H. Lin, C.W. Nan, J.L. MacManus-Driscoll, Dielectric films for high performance capacitive energy storage: Multiscale engineering, Nanoscale. 12 (2020) 19582–19591. https://doi.org/10.1039/d0nr05709f.

[34] X. Ren, Large electric-field-induced strain in ferroelectric crystals by point-defect-mediated reversible domain switching, Nat. Mater. 3 (2004) 91–94. https://doi.org/10.1038/nmat1051.

[35] T. Rojac, E. Khomyakova, J. Walker, H. Ursic, A. Bencan, BiFeO3 ceramics and thick films: Processing issues and electromechanical properties, in: B. Stojanovic (Ed.), Magn. Ferroelectr. Multiferroic Met. Oxides, Elsevier, Amsterdam, 2018: pp. 515–525. https://doi.org/10.1016/B978-0-12-811180-2.00024-4.

[36] G. Geneste, C. Paillard, B. Dkhil, Polarons, vacancies, vacancy associations, and defect states in multiferroic BiFeO3, Phys. Rev. B. 99 (2019) 24104. https://doi.org/10.1103/PhysRevB.99.024104.

[37] T. Shimada, T. Matsui, T. Xu, K. Arisue, Y. Zhang, J. Wang, T. Kitamura, Multiferroic nature of intrinsic point defects in BiFeO3: A hybrid Hartree-Fock density functional study, Phys. Rev. B. 93 (2016) 17410717. https://doi.org/10.1103/PhysRevB.93.174107.

[38] R. Schmidt, W. Eerenstein, T. Winiecki, F.D. Morrison, P.A. Midgley, Impedance spectroscopy of epitaxial multiferroic thin films, Phys. Rev. B. 75 (2007) 245111. https://doi.org/10.1103/PhysRevB.75.245111.

[39] S.H. Kim, J.H. Moon, J.H. Park, J.G. Park, Y. Kim, Analysis of defect formation in Nb-doped SrTiO3 by impedance spectroscopy, J. Mater. Res. 16 (2001) 192–196. https://doi.org/10.1557/JMR.2001.0031.

[40] J. Wu, J. Wang, Ferroelectric and impedance behavior of La- and Ti-codoped BiFeO 3 thin films, J. Am. Ceram. Soc. 93 (2010) 2795–2803. https://doi.org/10.1111/j.1551-2916.2010.03816.x.

[41] S. Cho, C. Yun, S. Tappertzhofen, A. Kursumovic, S. Lee, P. Lu, Q. Jia, M. Fan, J. Jian, H. Wang, S. Hofmann, J.L. MacManus-Driscoll, Self-assembled oxide films with tailored nanoscale ionic and electronic channels for controlled resistive switching, Nat. Commun. 7 (2016) 1–10. https://doi.org/10.1038/ncomms12373.

[42] H. Ishiwara, Impurity substitution effects in BiFeO 3 thin films - From a viewpoint of FeRAM applications, Curr. Appl. Phys. 12 (2012) 603–611. https://doi.org/10.1016/j.cap.2011.12.019.

[43] H. Pan, Q. Zhang, M. Wang, S. Lan, F. Meng, J. Ma, L. Gu, Y. Shen, P. Yu, Y.H. Lin, C.W. Nan, Enhancements of dielectric and energy storage performances in lead-free films with sandwich architecture, J. Am. Ceram. Soc. 102 (2019) 936–943. https://doi.org/10.1111/jace.16145.

[44] G.G. Raju, Dielectrics in electric fields, second edition, Taylor & Francis, Boca Raton, 2016. https://doi.org/10.1201/b20223.

[45] B. Ma, Z. Hu, R.E. Koritala, T.H. Lee, S.E. Dorris, U. Balachandran, PLZT film capacitors for power electronics and energy storage applications, J. Mater. Sci. Mater. Electron. 26 (2015) 9279–9287. https://doi.org/10.1007/s10854-015-3025-0.

[46] H. Cheng, J. Ouyang, Y.X. Zhang, D. Ascienzo, Y. Li, Y.Y. Zhao, Y. Ren, Demonstration of ultra-high recyclable energy densities in domain-engineered ferroelectric films, Nat. Commun. 8 (2017) 1999. https://doi.org/10.1038/s41467-017-02040-y.

[47] G. Catalan, J.F. Scott, Physics and applications of bismuth ferrite, Adv. Mater. 21 (2009) 2463–2485. https://doi.org/10.1002/adma.200802849.

[48] S. Cho, C. Yun, Y.S. Kim, H. Wang, J. Jian, W. Zhang, J. Huang, X. Wang, H. Wang, J.L. MacManus-Driscoll, Strongly enhanced dielectric and energy storage properties in lead-free perovskite titanate thin films by alloying, Nano Energy. 45 (2018) 398–406. https://doi.org/10.1016/j.nanoen.2018.01.003.

[49] N. Ortega, A. Kumar, J.F. Scott, D.B. Chrisey, M. Tomazawa, S. Kumari, D.G.B. Diestra, R.S. Katiyar, Relaxor-ferroelectric superlattices: High energy density capacitors, J. Phys. Condens. Matter. 24 (2012) 445901. https://doi.org/10.1088/0953-8984/24/44/445901.

[50] Y. Wang, X. Liu, H. Sun, H. Sui, C. Yan, Enhanced recoverable energy storage density of barium strontium titanate-based thin films with compositionally graded structure, J. Mater. Sci. Mater. Electron. 32 (2021) 2193–2199. https://doi.org/10.1007/s10854-020-04984-2.

[51] T.M. Correia, M. McMillen, M.K. Rokosz, P.M. Weaver, J.M. Gregg, G. Viola, M.G. Cain, A lead-free and high-energy density ceramic for energy storage applications, J. Am. Ceram. Soc. 96 (2013) 2699–2702. https://doi.org/10.1111/jace.12508.

[52] P. Chen, S. Wu, P. Li, J. Zhai, B. Shen, Great enhancement of energy storage density and power density in BNBT/xBFO multilayer thin film hetero-structures, Inorg. Chem. Front. 5 (2018) 2300–2305. https://doi.org/10.1039/c8qi00487k.

[53] H. Zhu, M. Liu, Y. Zhang, Z. Yu, J. Ouyang, W. Pan, Increasing energy storage capabilities of space-charge dominated ferroelectric thin films using interlayer coupling, Acta Mater. 122 (2017) 252–258. https://doi.org/10.1016/j.actamat.2016.09.051.

[54] M.D. Nguyen, E.P. Houwman, G. Rijnders, Energy Storage Performance and Electric Breakdown Field of Thin Relaxor Ferroelectric PLZT Films Using Microstructure and Growth Orientation Control, J. Phys. Chem. C. 122 (2018) 15171–15179. https://doi.org/10.1021/acs.jpcc.8b04251.

[55] X. Hao, Y. Wang, L. Zhang, L. Zhang, S. An, Composition-dependent dielectric and energy-storage properties of (Pb,La)(Zr,Sn,Ti)O3 antiferroelectric thick films, Appl. Phys. Lett. 102 (2013) 163903. https://doi.org/10.1063/1.4802794.

[56] Z. Hu, B. Ma, R.E. Koritala, U. Balachandran, Temperature-dependent energy storage properties of antiferroelectric Pb0.96La0.04Zr0.98Ti0.02O 3 thin films, Appl. Phys. Lett. 104 (2014) 263902. https://doi.org/10.1063/1.4887066.

[57] Y.Z. Li, Z.J. Wang, Y. Bai, Z.D. Zhang, High energy storage performance in Ca-doped PbZrO3 antiferroelectric films, J. Eur. Ceram. Soc. 40 (2020) 1285–1292. https://doi.org/10.1016/j.jeurceramsoc.2019.11.063.

[58] Z. Xie, Z. Yue, G. Ruehl, B. Peng, J. Zhang, Q. Yu, X. Zhang, L. Li, Bi(Ni1/2Zr1/2)O3-PbTiO3 relaxor-ferroelectric films for piezoelectric energy harvesting and electrostatic storage, Appl. Phys. Lett. 104 (2014) 243902. https://doi.org/10.1063/1.4884427.

[59] H. Pan, Y. Zeng, Y. Shen, Y.H. Lin, J. Ma, L. Li, C.W. Nan, BiFeO3-SrTiO3 thin film as a new lead-free relaxor-ferroelectric capacitor with ultrahigh energy storage performance, J. Mater. Chem. A. 5 (2017) 5920–5926. https://doi.org/10.1039/c7ta00665a.